Railway Engineering Science (2024) 32(2):162–176
https://doi.org/10.1007/s40534-023-00324-2

A framework for dynamic modelling of railway track switches considering the switch blades, actuators and control systems

Saikat Dutta[1] · **Tim Harrison**[2] · **Christopher Ward**[2] · **Roger Dixon**[3] · **Phil Winship**[4]

Received: 3 May 2023 / Revised: 15 August 2023 / Accepted: 6 October 2023 / Published online: 9 January 2024

Abstract

The main contribution of this paper is the development and demonstration of a novel methodology that can be followed to develop a simulation twin of a railway track switch system to test the functionality in a digital environment. This is important because, globally, railway track switches are used to allow trains to change routes; they are a key part of all railway networks. However, because track switches are single points of failure and safety-critical, their inability to operate correctly can cause significant delays and concomitant costs. In order to better understand the dynamic behaviour of switches during operation, this paper has developed a full simulation twin of a complete track switch system. The approach fuses finite element for the rail bending and motion, with physics-based models of the electromechanical actuator system and the control system. Hence, it provides researchers and engineers the opportunity to explore and understand the design space around the dynamic operation of new switches and switch machines before they are built. This is useful for looking at the modification or monitoring of existing switches, and it becomes even more important when new switch concepts are being considered and evaluated. The simulation is capable of running in real time or faster meaning designs can be iterated and checked interactively. The paper describes the modelling approach, demonstrates the methodology by developing the system model for a novel "REPOINT" switch system, and evaluates the system level performance against the dynamic performance requirements for the switch. In the context of that case study, it is found that the proposed new actuation system as designed can meet (and exceed) the system performance requirements, and that the fault tolerance built into the actuation ensures continued operation after a single actuator failure.

Keywords Railway track switch · Mathematical modelling · Redundant actuation · Finite element analysis

1 Introduction

Track switch systems, which enable the rail vehicle to change tracks, are critical assets of any rail network. A single fault in the existing track switch systems can result in a delay in the network or even lead to catastrophic accidents. Bemment et al. [1] studied the effect of failure in the switch system and its effect on the UK rail network from historical data. Ref. [1] showed that, although the switches account for less than 5% of the rail network in terms of track miles, they contribute 18.3% of delay minutes and 17.6% delay costs in the UK within the period of study.

There are two main approaches being taken to improve the reliability and availability of track switch systems. Firstly, research and development applied a condition monitoring approach to predict faults and failures and use predictive maintenance to avoid them [2–6]. Secondly, researchers are working to develop completely new track switching concepts [7–10], which include dramatically changing the layout (of the rails) and the motion of the moving elements of the track. However, testing of monitoring or new switches in the real environment is extremely expensive (and potentially dangerous); so, an issue in both cases is the lack of tools to appropriately simulate the behaviour of track switch systems. Simulation

✉ Saikat Dutta
s.dutta@leeds.ac.uk

[1] Institute of Thermofluids, School of Mechanical Engineering, University of Leeds, Leeds, West Yorkshire, UK

[2] Wolfson School of Mechanical, Electrical and Manufacturing Engineering, Loughborough University, Loughborough, Leicestershire, UK

[3] Birmingham Centre for Railway Research and Education, School of Engineering, University of Birmingham, Birmingham, West Midlands, UK

[4] Network Rail, Milton Keynes, Buckinghamshire, UK

can significantly reduce upfront costs, demonstrate the viability of new methods and concepts, and in doing so expedite progress through the technology readiness levels.

Simulation tools and models which allow a comprehensive assessment of switches and their actuation mechanisms are rare and those which are available are limited in their utility. The most common track switch simulations look at the wheel–rail interface exploring the forces between wheel and rail as vehicles pass over the switch [11–14]. Whilst this is important (especially with new layouts), it gives no useful information about how the switch moves during switching, which is important for understanding the design of the switch, machine (actuator), and its associated control system. Anecdotal evidence from engineers in UK and Europe indicates that a limited steady-state analysis is used for the sizing and design of track switches and placement and sizing of actuators. In the research community finite element (FE) models are used [15, 16] for static bending, but are not able to check the dynamic performance when connected to actuation and control elements. Recent work [10, 17] has considered the use of co-simulation and to allow integration of a classical (1D) switch model with the actuator and the control models; but this co-simulation required the use of at least two software packages and run-times were very slow, making it almost unusable. One article has studied a 2D finite element analysis to explore the possibilities of redundancy [18]. However, no other research has been found using multibody/dynamic simulation packages to model the dynamic movement of the entire switch.

In this paper, an innovative approach is proposed to generate a single dynamic simulation model of the complete track switch system. The model fuses finite element methods for rail bending and motion with physics-based models of the electromechanical actuator system and the control system. The entire model can be implemented in a single software; for example, MATLAB/Simulink™. A key enabler is a finite element model of the rails (FE-Rail) which is developed considering each rail as a 3D cantilever Timoshenko beam element [19, 20]. Importantly, this model can be implemented in MATLAB/Simulink™ alongside the dynamic models of the actuation and control system elements. Since the rail model discussed here allows movement in 3D, the approach can be used to evaluate the new switch motions currently emerging in the literature and industry. The methodology is demonstrated in this paper by developing a simulation twin for the REPOINT switch concept [9] which includes a redundant actuation system and a new way of actuation (lift-hop-drop) and locking. The simulation twin of this REPOINT system is tested for performance versus requirements.

The remainder of this paper is set out as follows. In the second section, the mathematical modelling of the switch blades (designated, FE-Rail) is presented, along with the validation of this model against the steady-state analytical solution. Thereafter, the models of the electromechanical actuation system are described and these models are integrated. In Sect. 3, the controller requirements and design approach are presented. The performance vs requirement of the entire closed-loop switch system is examined in Sect. 4, both in the fault free (normal operation) case (A) and in the case of two (out of three) faulty actuators (B).

2 Mathematical modelling

2.1 Switch system layout

The schematic of the switch system being modelled is shown in Fig. 1. In this layout, the traditional stock rails and switch rails are replaced and redesigned as stub rails with uniform cross sections to allow for a novel actuation movement, as described by Bemment et al. [21, 22]. The stub switch rails are moved in a semi-circular arc to achieve the switching motion [9, 10]. This switch system operates with multiple actuators (shown as active bearers in the layout) to introduce redundancy into the switch system. The different components of the actuation mechanism are shown in Fig. 2. In Fig. 1, the dotted rails represent the switch position after the switching operation (to take the turnout route). Here, a three-dimensional finite element model of the rail, FE-Rail, is developed first and the steady-state response of the dynamic rail bending analysis is validated against the analytical solution in Sect. 2.2. The three actuators, shown by the red lines in Fig. 1, are modelled in Sect. 2.3 and integrated into the FE-Rail model.

2.2 FE-rail model development

In this section, the FE-Rail model is developed considering the stub switch rail as a cantilever beam fixed at one end (Fig. 3). The FE-Rail is modelled as a cantilever beam because of this new stub switch layout with the new actuation method. When the switch is in operation, the rails are not in contact with the sleepers and fasteners, and the rails are only fixed at one end (from position 11 in Fig. 1. In addition, the FE modelling does not include the crossing section of the switch as this does not impact the movement (or bending) of the rails; only movable length of the stub switch rails is considered. This lift-hop-drop actuation system also means that it is reasonable to ignore interactions, such as friction, between the movable rails and the fixed rails. This would be needed for a conventional switch system, but is negligible here.

The general layout and dimensions of the stub switch layout are designed based on the network rail drawing for an NR60 inclined C-switch (REPW2001). The movable stub switch rails are shown as two rails (shown as side A and side B in

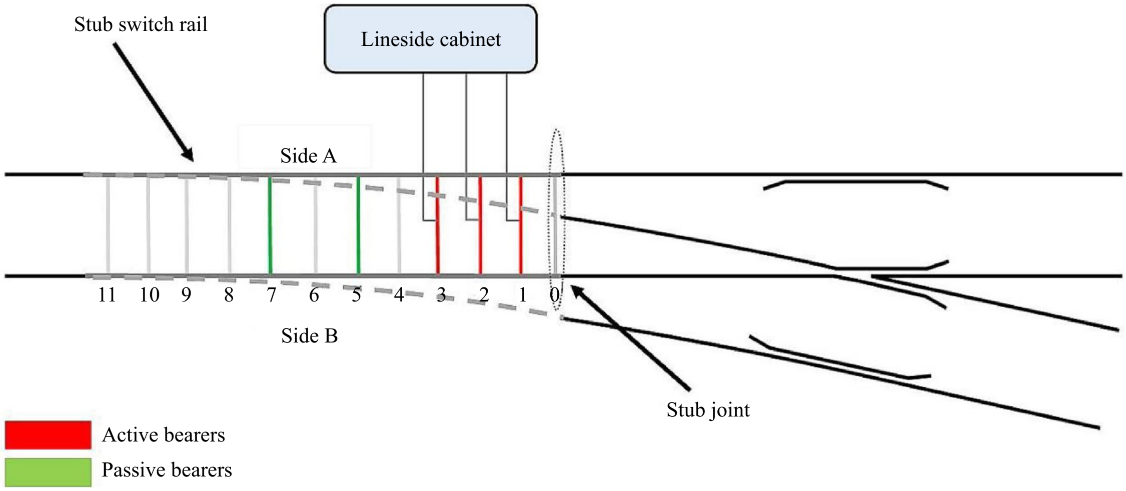

Fig. 1 Schematic diagram of the new switch mechanism showing rail elements and actuators

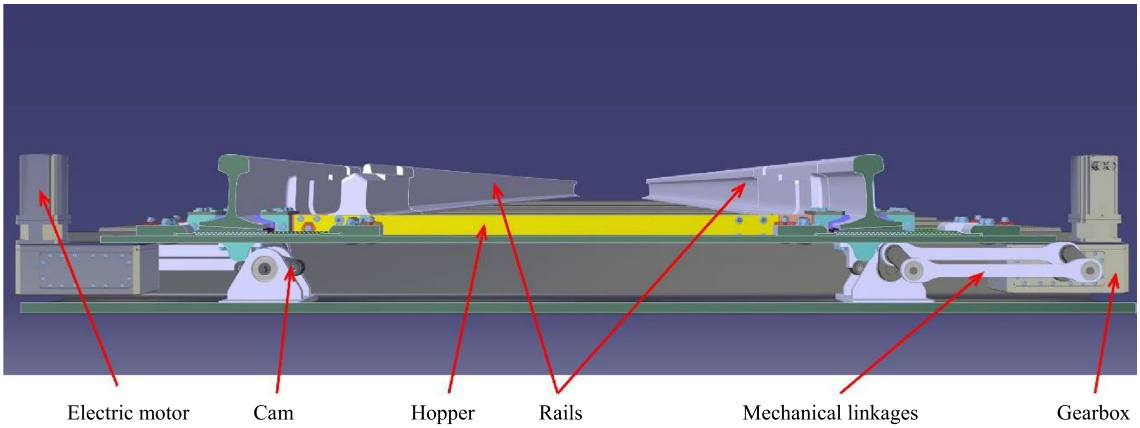

Fig. 2 Single actuator bearer

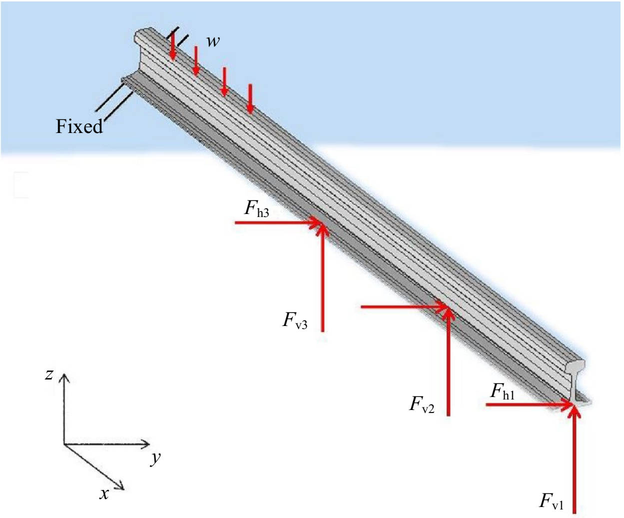

Fig. 3 The rail element and the forces acting on it

Fig. 1), and the length of both movable beam elements (L) is 7800 mm. In a conventional switch C-layout, the switch rail cross section varies along the length of the rail. However, in the stub switch layout, the switch rail cross section remains constant with the free end of the rails terminating in stub joints (as shown in Fig. 1). The rail cross section area and steel density (mass) are standard values assuming NR60 rail (as used in much of the UK rail network). The two rails are modelled as two separate beams, and in this section, the analysis of a single FE-Rail (single beam) is presented. The properties of the other beam (side B of Fig. 3) are identical. The beam is divided into N elements (as shown in Fig. 4a), each of equal length ($l = L/N$). The nodes of the finite body are denoted by the black dots and numbered in red; the element numbers are given in blue in the boxes. For example, element 2 has nodes 1 and 2. One element with two nodes is shown in Fig. 4b. Each node of the element has six degrees of freedom.

The nodal displacement vector for the element 1 in the local coordinate system as shown in Fig. 4b is

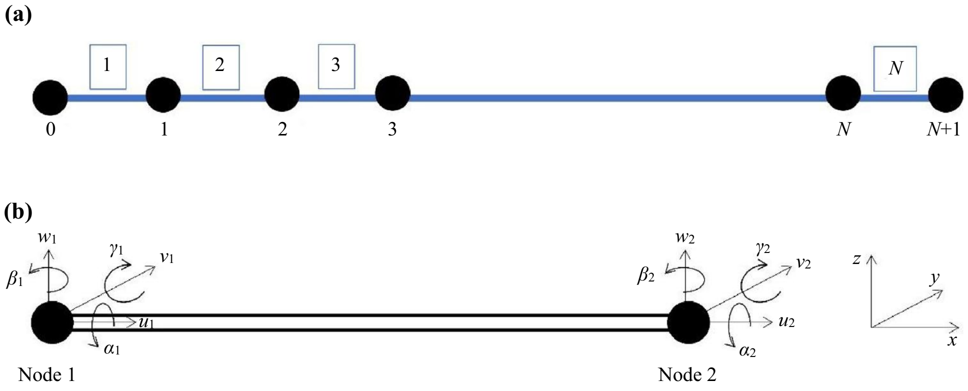

Fig. 4 FE-rail model development: **a** showing N elements; **b** one element with the degrees of freedom

$$\boldsymbol{u}_1^e = (u_1,\ v_1,\ w_1,\ \alpha_1,\ \beta_1,\ \gamma_1,\ u_2,\ v_2,\ w_2,\ \alpha_2,\ \beta_2,\ \gamma_2)^{\mathrm{T}}. \quad (1)$$

The individual mass and stiffness matrices of one element, element e are generated as $\boldsymbol{M}^e$ and $\boldsymbol{K}^e$ following Eq. (2) [20, 23]. The full equations are listed in Appendix. The two nodes of the element e are denoted as 1 and 2, respectively. Each element consists of two nodes and each node of the element has six degrees of freedom (Fig. 4b). The size of the matrices $\boldsymbol{M}^e$ and $\boldsymbol{K}^e$ is 12×12, which is the degrees of freedom of the element e. The individual matrices (such as $\boldsymbol{M}_{11}^e$) are of the order 6×6 considering the six degrees of freedom at the nodes. $\boldsymbol{M}_{11}^e$ and $\boldsymbol{M}_{22}^e$ correspond to the independent nodes, and $\boldsymbol{M}_{21}^e$ and $\boldsymbol{M}_{12}^e$ correspond to interdependencies of the nodes.

$$\boldsymbol{M}^e = \begin{bmatrix} \boldsymbol{M}_{11}^e & \boldsymbol{M}_{12}^e \\ \boldsymbol{M}_{21}^e & \boldsymbol{M}_{22}^e \end{bmatrix}, \quad (2)$$

$$\boldsymbol{K}^e = \begin{bmatrix} \boldsymbol{K}_{11}^e & \boldsymbol{K}_{12}^e \\ \boldsymbol{K}_{21}^e & \boldsymbol{K}_{22}^e \end{bmatrix}. \quad (3)$$

These element-wise mass and stiffness matrices are used to generate the global mass and stiffness matrices, as $\boldsymbol{M}_{\mathrm{F}}$ and $\boldsymbol{K}_{\mathrm{F}}$, respectively. As the elements are chosen as sections of rail, no coordinate transformation is needed during the assembly of the FE-Rail model.

As the rail end is fixed at one end (at node 0, Fig. 4a), the deflections and slope at that node will be zero. Thus, for the bending analysis, the first six rows and columns (corresponding to node 0) are dropped and the global matrices of the rail element are obtained as $\boldsymbol{M}$ and $\boldsymbol{K}$ (both of size $6N \times 6N$). The equations on how the global matrices for the FE-Rail body are assembled are shown in the Appendix.

The global state vector is obtained as

$$\boldsymbol{u} = (u_1,\ v_1,\ w_1,\ \alpha_1,\ \beta_1,\ \gamma_1,\ u_2,\ \cdots,\ u_N,\ v_N,\ w_N,\ \alpha_N,\ \beta_N,\ \gamma_N)^{\mathrm{T}}. \quad (4)$$

The force vector is a vector of size $6N$, which also include the weight of the elements. The weight (w) of individual elements is included in the third element of the elemental force vector. The element size is selected in a way that the actuation points (active bearer positions, shown in red in Figs. 1 and 3) coincide with the nodes of the finite body. For the analysis, active forces are added to the corresponding nodes in the force vector. Thus, the global force vector $\boldsymbol{F}$ is obtained as

$$\boldsymbol{F} = (0,\ -w,\ 0,\ 0,\ 0, \cdots, 0,\ F_{\mathrm{h3}},\ -w, +F_{\mathrm{v3}},\ 0,\ 0,\ 0,\ \cdots,\ 0,\ F_{\mathrm{h1}},\ -w, +F_{\mathrm{v1}},\ 0,\ 0,\ 0)^{\mathrm{T}}. \quad (5)$$

The damping is considered to be proportional Rayleigh damping [24, 25] as in Eq. (6). The two coefficients ϕ_1 and ϕ_2 are usually obtained from experimental results. However, for steels, the values can be approximated to match the static solution.

$$\boldsymbol{D} = \phi_1 \boldsymbol{M} + \phi_2 \boldsymbol{M}. \quad (6)$$

The equation of motion of the finite rail body is obtained as,

$$\boldsymbol{M}\ddot{\boldsymbol{u}} + \boldsymbol{D}\dot{\boldsymbol{u}} + \boldsymbol{K}\boldsymbol{u} = \boldsymbol{F}. \quad (7)$$

The FE-Rail model is then developed in MATLAB/Simulink™. The steady-state deflection of the FE-Rail from the dynamic simulation is validated against the analytical static solution of the beam when subjected to vertical or horizontal forces. The various parameters of the rail elements were obtained from the network rail drawing for NR60 C-switch (REPW2001) and listed in Table 1. It should be noted here that on a PC, this model could run a 12-s simulation in 10 s.

2.2.1 Bending of rail when subjected to a single force at position 1 (node *N*+1)

To check the deflection in each direction independently, the deflection of the rail when subjected to a single force at a single position is considered. The static deflection can

Table 1 Parameters of the actuation elements

Parameter	Definition	Value	Parameter	Definition	Value
m_R	Mass of rail (1 m length)	60 kg	m_1	Mass of each element	$m_\mathrm{R}L/N$
L	Length of the movable rail	7.8 m	N	Number of elements	33
I_y	Moment of inertia about y	512.3 cm^4	I_z	Moment of inertia about z	3038.3 cm^4
I_p	Polar moment of inertia	2032.0 cm^4	A	Cross-section area	7670 mm^2
l	Length of single element	L/N	I_t	Torsion constant	2.16×10^6 m^4
E	Young's modulus of steel	$200\times10^9\ \mathrm{N/m}^2$	G	Shear modulus	$\frac{E/2}{1+\nu}$
ν	Poisson's ratio	0.3	ϕ_1	Coefficient of Rayleigh damping 1	10^{-6}
ϕ_2	Coefficient of Rayleigh damping 2	8			

Table 2 Validation of the force needed for a given displacement at bearer 1 position (force acting at position 1 only)

Deflection (mm)	Analytical solution (N)	FE-Rail (N)	Error (%)
Horizontal direction			
8.92	66	69	4.5
33.30	246	257	4.4
66.60	493	513	4.0
99.90	739	760	2.9
124.28	920	938	1.9
133.2	986	1007	2.1
Vertical direction			
11.57	2564	2573	0.3
33.30	3648	3596	1.4
51.02	4531	4475	1.25
62.58	5108	5004	2.1
66.60	5308	5287	0.4

Table 3 Test case studies for validation work

Case #	Bearer 1	Bearer 2	Bearer 3
1	Active	Active	–
2	Active	–	Active
3	–	Active	Active
4	Active	Active	Active

be obtained analytically using the Euler–Bernoulli beam bending equations of a cantilever beam. The static deflection (analytically obtained) and the steady-state deflection of the FE-Rail model are listed in Table 2.

For this case, a horizontal force at position 1 (Fig. 3) is only active to validate the results for the horizontal direction. Similar results are obtained for vertical direction when only vertical force in position 1 is active. The force required for different deflection magnitudes is compared. For the switching operation, the maximum deflection of the rail (or the throw of the stub switch rail) at position 1 is 133.2 mm in the horizontal direction and the maximum vertical movement at this position is 66.6 mm. It is seen from Table 2 that the horizontal force values for the FE-Rail match well with the analytical solution. Although the magnitude of the vertical forces for FE-Rail differs from the analytical solution, the maximum error is 2.1% of the analytical solution.

2.2.2 Rail bending with multiple forces applied

Since, in normal operation, forces will be applied to both rails from all three bearers, here validation in this scenario is considered. The different test case combinations of forces acting on three bearer positions are listed in Table 3. During normal operation, all three actuators will be active and forces act on the rails in different positions in vertical and horizontal directions. The amplitude of the force applied is set at 2000 N in the vertical direction and 500 N in the horizontal direction at each bearer on each rail.

The steady-state deflection profile of the FE-Rail is validated against the steady-state response from the analytical solution (Fig. 5). The error in the displacement at the tip of the rail (bearer 0 positions of Fig. 1) between the two results is tabulated in Table 4. It can be seen that the maximum error is negligible in the horizontal direction. However, the error in FE-Rail and analytical solution is a maximum of 3.63% from the analytical solution in the vertical direction when three bearers are active. However, the movable length of the rail is 7.8 m, and the maximum error in the vertical direction (i.e. 1 mm) is almost negligible.

After validating the FE-model against the analysis solution, the FE-Rail model is used to determine the opening of the rails at bearer positions, which is obtained as 133.2 mm at bearer 1, 56.2 mm at bearer 2, and 47.2 mm at bearer 3. In the next section, the movement of the rails was checked for these opening magnitudes.

This validated FE-Rail model can be used for any kind of switch motion, with possible modification depending on the switch profile and actuation system. In the following sections, the FE-Rail model will be attached to the lift-hop-drop actuation mechanism to complete the simulation twin.

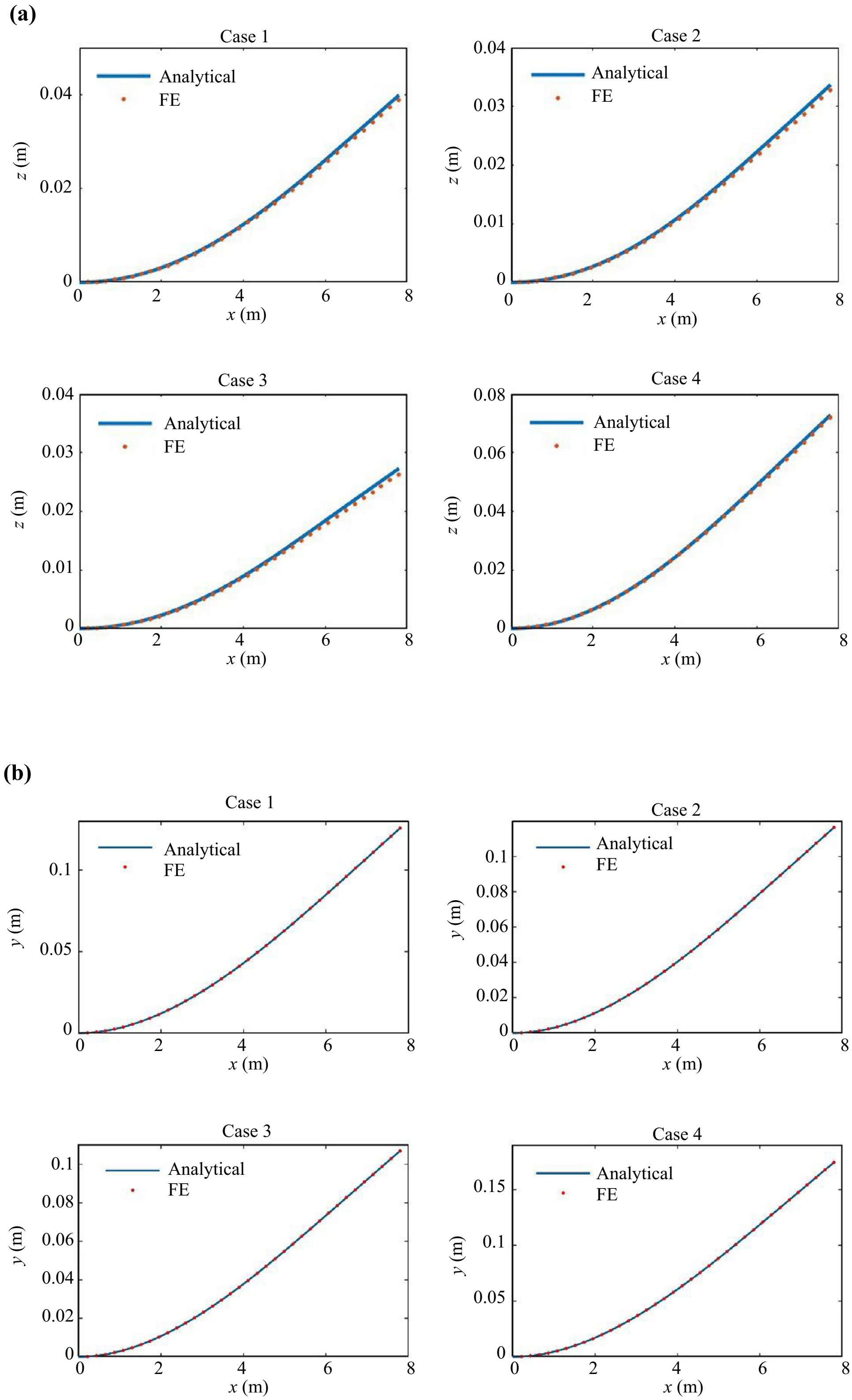

Fig. 5 Validation of FE model with the analytical solution—for REPOINT force cases: **a** vertical deflection; **b** horizontal deflection

Table 4 Validation under actuator force scenarios

Case #	Max disp. (FE-Rail) (mm)	Max disp. (analytical) (mm)	Error (mm)	Error from analytical solution (%)
Horizontal direction				
1	125.65	125.64	−0.01	−0.008
2	116.42	116.40	−0.02	−0.017
3	106.93	106.90	−0.03	−0.028
4	174.51	174.49	−0.02	−0.011
Vertical direction				
1	38.94	39.92	0.98	2.45
2	32.72	33.7	0.98	2.91
3	26.31	27.3	0.99	3.63
4	71.91	72.87	0.96	1.32

2.3 Actuation system model

As mentioned earlier, there are three actuator bearers positioned as per Fig. 1. A diagram of one such bearer can be seen in Fig. 2. From Fig. 2, it can be seen that each actuator consists of two independent electrical motor and gearbox systems connected to the cam through some mechanical linkages. The hopper is moved with the cams and the rails are supported on the hopper. The electric motor and gear box parameters are given in Table 5. The inputs to the actuation system are the commanded voltage and the load (from the hopper) on the cams. The electric motor and gearbox assembly rotates the cam which is connected through some mechanical linkages to the gearbox output shaft. The cam position output is fed to the control system along with the speed and current of the electrical motor. The control system is developed in the next section. The governing equations for the actuation elements are derived using physical laws.

The electrical equation of a motor is derived as

$$V_{\mathrm{M}} = iR + L_{\mathrm{a}}\dot{i} + K_{\mathrm{b}}\dot{\omega}_{\mathrm{M}}, \tag{8}$$

$$T_{\mathrm{M}} = K_{\mathrm{T}}i, \tag{9}$$

where V_{M} is the voltage to the motor, T_{M} is motor electrical torque, i is the armature current, and ω_{M} is the motor speed. The parameters of the motor are listed in Table 5. The effect of the short connecting shaft between the motor and gearbox and the backlash of the gearbox is neglected in this study, and the governing equation of the combined system is derived as

$$(J_{\mathrm{M}} + J_{\mathrm{GH}})\ddot{\theta}_{\mathrm{M}} + (B_{\mathrm{M}} + B_{\mathrm{GH}})\dot{\theta}_{\mathrm{M}} = T_{\mathrm{M}} - T_{\mathrm{go}}/n_{\mathrm{GH}}, \tag{10}$$

where θ_{M} is the rotational displacement of the motor. The gearbox output speed (ω_{gh}) and the motor speed or the gearbox input speed (ω_{M}) are related as $\omega_{\mathrm{M}} = n_{\mathrm{GH}}\omega_{\mathrm{go}}$, in which ω_{go} is gearbox output speed. The output shaft of the gearbox is connected to the cam through rigid mechanical linkages. The inertia of the linkages is considered as a lumped mass on the cam. The shaft connector between the gearhead output and the cam is considered as rigid so that the relative motion between these two doesn't exist. Thus, the torque of individual cam from the gearbox is calculated as

$$T_{\mathrm{go}} = K_{\mathrm{GH}}(\theta_{\mathrm{go}} - \theta_{\mathrm{C}}), \tag{11}$$

and the governing equation of the cam is calculated as

$$J_{\mathrm{C}}\,\ddot{\theta}_{\mathrm{C}} + B_{\mathrm{C}}\,\dot{\theta}_{\mathrm{C}} = T_{\mathrm{go}} - T_{\mathrm{L}}, \tag{12}$$

where T_{L} is the load acting on the cam from the hopper, θ_{go} is gearbox output angular position, and θ_{C} is cam angle. The actuator model contains two of these motors, gearboxes, linkages and cam models one on the left-hand side and one on the right-hand side as shown in Fig. 2.

2.4 Integration of rail and actuator model

The cam of the actuator model supports the hopper of the switch panel. The connections between the cam and hopper are modelled as a stiff spring and damper to ensure support. However, these connections are switched off when the force between the hopper and the cam is negative, allowing the model to represent the lifting of the hopper without the cam, which is possible when the individual cam is not in operation. Also, in this actuation scenario, it is possible that in any instance of time, one cam (or more than one) does not support the hopper. This discontinuation in the connection is also modelled such that if the rail position is not in contact with the cam, the connection is lost.

The two rails are connected to each other and to the hoppers at the three bearer positions. In the SIMULINK™ model, these two rails are connected by stiff connections which represent the hopper at those positions to prevent any relative movement. The full switch model is developed in MATLAB/Simulink™ as shown in Fig. 6.

Table 5 Parameters of the actuation elements

Parameter	Definition	Value
B_{C}	Cam frictional coefficient	0.004 Nm/(rad/s)
B_{GH}	Gearhead frictional coefficient	1.91×10^{-5} Nm/(rad/s)
B_{M}	Motor frictional coefficient	4.01×10^{-4} Nm/(rad/s)
J_{C}	Cam inertia	0.004 kg·m^2
J_{GH}	Gearhead inertia	6.28 kg·m^2
J_{M}	Motor inertia	2.16 kg·m^2
K_{GH}	Rotational Stiffness of the gearhead	41,250 Nm/rad
K_{b}	Back emf constant	0.441 V/(rad/s)
K_{T}	Motor torque constant	0.72 Nm/A
L_{a}	Motor inductance	2.7 mH
n_{GH}	Gear ratio	20
R	Rotor resistance	0.54 Ω

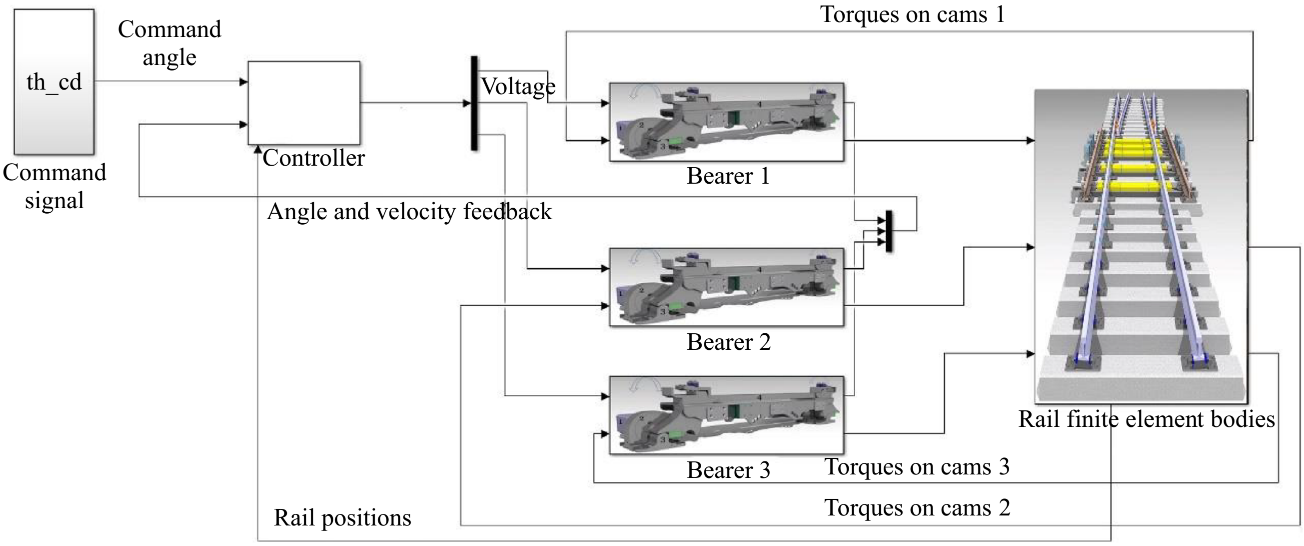

Fig. 6 Full switch model developed in MATLAB/Simulink

3 Control system design

The control system of the switch system is required to provide accurate angular position control as shown in the Fig. 7. The command signal in the form of a cam angle command is fed to the individual motor controller within the actuator bearer. Each bearer houses two motors which are connected to the rails through the other actuator elements. The two motors in actuator bearer 1 are referred to as B1M1 and B1M2, where B1 refers to the bearer number 1 and M1 and M2 refer to the rail side, i.e. side 1 and side 2, respectively, from Fig. 1. The angular positions of the cams are 0° at the position shown in the schematic diagram (Fig. 1). After the switching operation, the rails move to the other position and the cam angle positions become 180°. Hence, in the present controller, the command angle to the control system is between 0° and 180° depending on the switching requirement.

As per Fig. 7, the actuation is controlled via three cascaded loops. The current controller in the innermost loop is designed first, and then the velocity controller in the middle loop is designed. The outermost loop position controller is designed last. The overall control algorithm needs to satisfy the requirements listed below.

Phase margin	$> 60\ ^\circ$
Gain margin	> 6 dB
Rise time	< 2 s
Settling time	< 4 s
Overshoot	$< 1\ \%$
Maximum current in a motor	< 20 A

The controllers are selected as proportional–integral (PI) controllers. The control input (u_{c}) for the PI controller is designed as

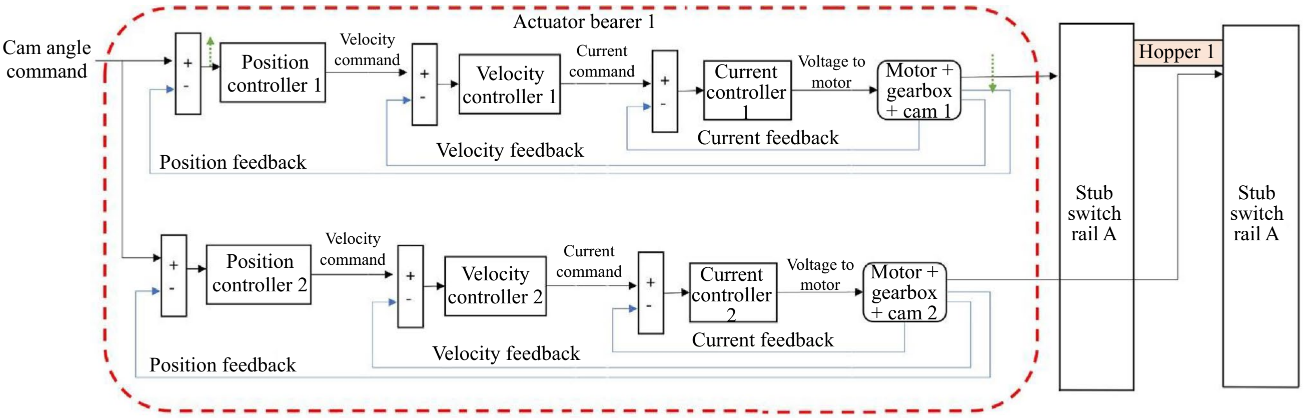

Fig. 7 Controller for a single bearer

$$u_c = K_P\varepsilon + K_I\int_{t_0}^{t}\varepsilon \mathrm{d}t. \tag{13}$$

where K_p and K_I are the proportional and integral gain, respectively, and ε is the error between the command signal and feedback signal. For example, for the current controller, the e is the error between the current command from the velocity controller and the motor current feedback.

It should be noted here that it is feasible to design a faster controller depending on the need for dynamic performance. During tuning the parameters of the cascading controller, different combinations of controller gains are selected, which are stable. The dynamic performance of the system is presented in Table 6 and shown in Fig. 8. The closed-loop performances at cam 1 or bearer 1 motor 1 are shown here. The cam 2 performance is identical, and the performance of the other actuator bearers is very similar in shape. However, bearer 1 does experience the largest loads (and hence currents). All three designed controller options (C_1, C_2 and C_{final}) satisfy all the control requirements. However, C_1 and C_2 produce significantly higher peak currents in the system when compared with C_{final}; these currents are in excess of 80% of the maximum allowable current in the motor. Hence, although the response time performance of the C_{final} is slower than that of the former controllers, it still satisfies the rise time and settling time requirements with a lower peak current.

The frequency responses of the system are performed using the Control Design toolbox in Simulink, and the input and output measurement points to design the outer loop (i.e. position controller) are indicated by the green arrows in Fig. 7. To ensure robustness of the control system after faults (e.g. one bearer fails), suitable stability margins are required (see requirements). The designed controller is designed to meet these, and the Nichols chart is plotted here in Fig. 9. From the open-loop frequency response of the chart, the gain and phase margins for the closed-loop system can be measured. Note that these gain and phase margins are the two most common indicators used by control engineers to show the stability of the system; for more information, see, for example, Refs. [26, 27]. The Nichols plot for the outermost loop with tuned internal loops is shown in Fig. 9 which shows that the gain margin is 38.8 dB and the phase margin is 88.6 ° which are well above the control requirements and ensures that the controller is stable and robust to perform in presence of any disturbances.

In the control requirements listed above, the allowable overshoot of 1% is permitted because the cams are allowed to rotate freely for this small movement (less than 2°) when the rails are locked in position without causing any hazard.

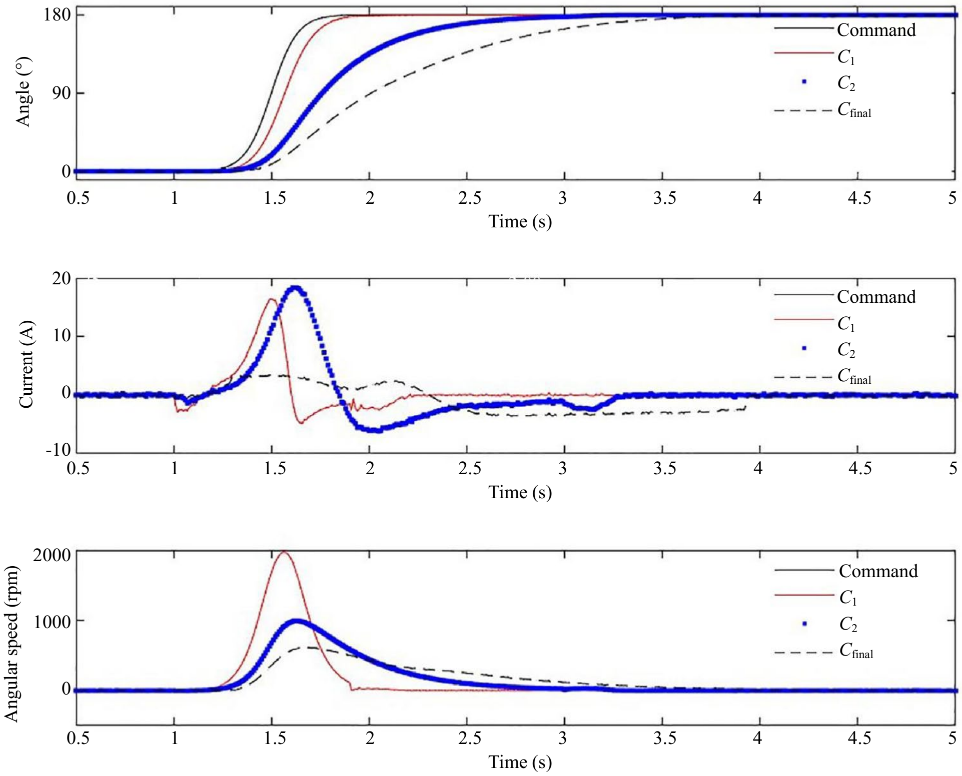

Fig. 8 Dynamic performances of the three designed controllers

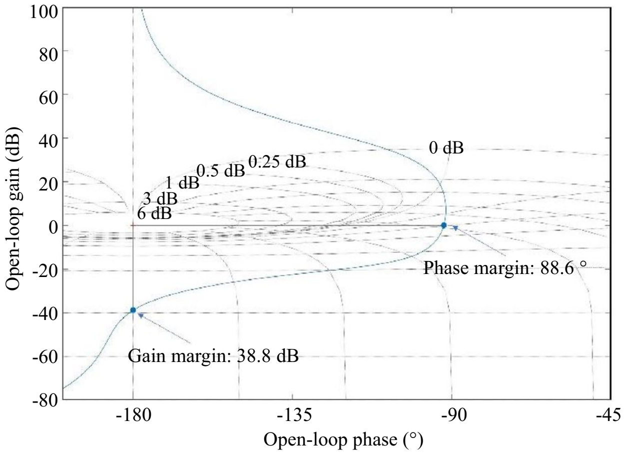

Fig. 9 Nichols plot to show stability margins

Also, upon receiving the switching command, the angle command is converted to sigmoid command from step command to eliminate potential high motor voltage at the initial period of the switching operation.

4 Performance evaluation of the switch

The actuation system is designed such that the switching operation can be carried out satisfying all the requirements. In this section, the results are shown for two operation scenarios: first when all three actuators are working and second when any single actuator is operating. In the real working environment, any individual actuator can experience fault and stops operating. In this situation, the other actuators can carry on performing till the failed actuator is replaced or repaired.

4.1 Operating with three actuators

The performance of the REPOINT actuator when all the bearers are working is shown in Fig. 10. There are six motors in the REPOINT system. The angle, current and velocity signals from the two motor-cam assemblies of any bearer are similar. Thus, the signals from side A (as shown in Fig. 1) are plotted in this figure to show the performance. The system is commanded to move from position 0° to 180° at time 1 s and again to 0° at time 6 s. Figure 10a shows that cam angles reach their desired positions at 2.03 s. Figure 10a also shows that the maximum current in B1M1 is 8.7A, which is below the maximum allowable range (20A as per requirement).

Table 6 Dynamic performance evaluation of designed controller

Parameter	C_1	C_2	C_{final}
Gain margin (dB)			38.8
Phase margin (%)			88.6
Rise time (s)	0.33	0.8	1.3
Settling time (s)	0.9	1.6	2.03
Maximum current in a motor B1M1 (A)	16.5	18.4	8.7

Figure 10b shows the displacement and movements of the rails. The plots ensure that the maximum lift and the horizontal movement satisfy the switching requirements.

4.2 Operating with single actuator

The selected controller parameters are used to check the system performance when operating with a single actuator bearer (B1) driving the entire switch (i.e. one actuator responsible for the entire load and switching operation). No power is provided to the motors of the other two actuators to ensure the non-operation of those actuators. The performance of the system is shown in Fig. 11. Although the switching command is a step signal which changes instantaneously from 0° to 180°, the command is changed to a sigmoidal command (command angle in Fig. 11a) to eliminate a sharper peak at the start. The cam angle plot shows that the cam angle settles at the commanded position of 180° after 2.36 s, which is well below the requirement of throw time or the settling time. Also, the current plot demonstrates that the maximum current is kept below the maximum current specified (i.e. 20 A).

The rail displacements in Fig. 11b show that the rails are switched to the position required when the switching occurs, and the vertical lifts also satisfy the cam radius requirements. For bearer 2 and bearer 3, the maximum lift is 56.2 and 47.2 mm, respectively, which are more than the lift required to clear the movements of the actuation elements (55.2 and 44.9 mm, respectively).

4.3 Failure case: one actuator failure in mid-operation

In this test case, one failure case is considered where one actuator fails midway through the operation. The fault case is created in the simulation environment. A fault is identified in the actuator mechanism in bearer 1 position at time 1.8 s (i.e. 0.8 s into the operation) during the operation. The designed controller discontinues the power to the motor instantaneously. The designed control system allows the other two actuators (bearer 2 and bearer 3) to complete the task. The dynamic response of the system is shown in Fig. 12. Figure 12a shows the dynamic performance of the motor and cams of side A of each bearer, which is marked as M1 for the three bearers. It can be seen from Fig. 12a that the current to the motor B1M1 becomes zero at time 1.8 s (the time of fault occurrence), and the angular speed of the cam at that position also reduces to zero. However, due to the redundancy of the actuation system, the other two bearers

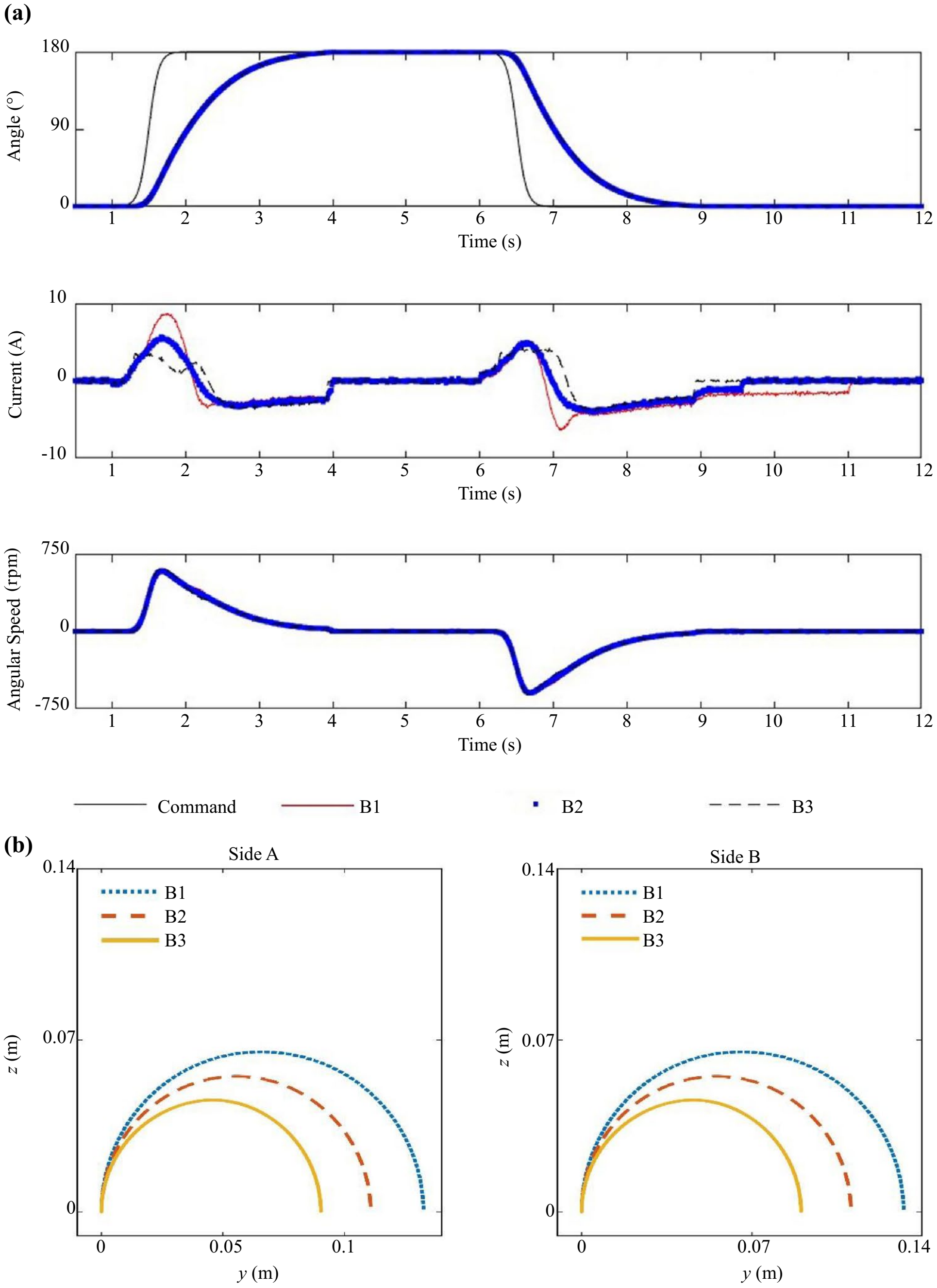

Fig. 10 Performance of the switch when operating with three actuators: **a** actuator performances; **b** movement of the rails at bearer positions

(B2 and B3) continue to operate, and a rise in the current in the case of B2M1 and B3M1 can be observed. The maximum current in the motor B2M1 becomes the highest among the bearers at 11.6 A, which satisfies the control requirement (< 20 A). It can also be noted that the settling time of this operation is 2.67 s, which is more than that of the normal operating case, but satisfies the control requirement (<4 s).

The rail displacement plot (Fig. 12b) shows that despite the failure of bearer 1 the rails are moved to the desired position as the two remaining bearers were able to perform the task. A sudden change in the movement behaviour can be noticed before halfway through the operation, which is the fault occurrence time.

5 Conclusions

The paper has proposed and presented a new approach to modelling a railway track switch which combined all the key elements of a dynamic simulation twin. The rail deflection, actuation mechanisms and control system have been combined and implemented in a single software platform,

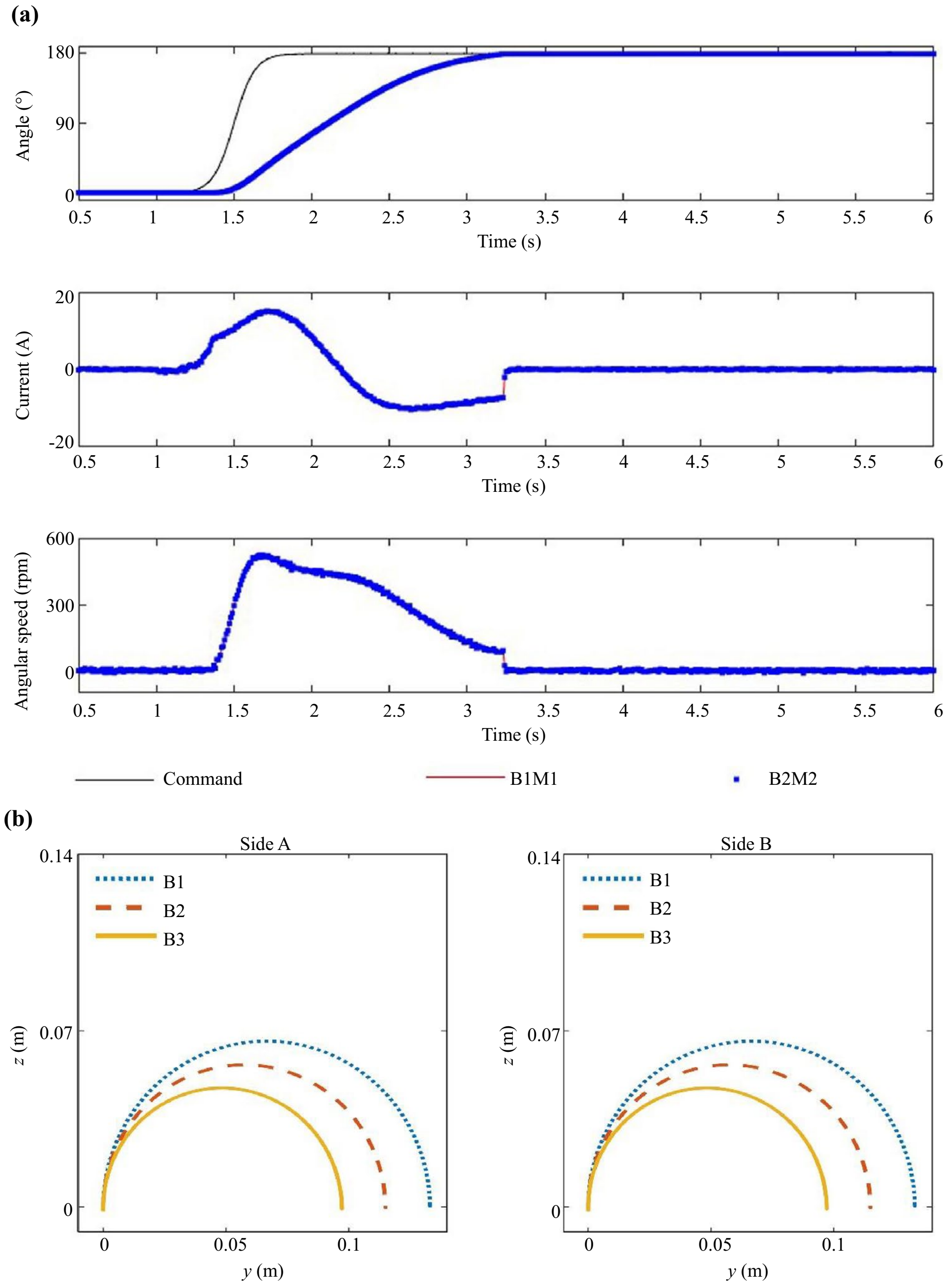

Fig. 11 Performance of the switch when operating with a single actuator (B1): **a** actuator performances; **b** movement of the rails at bearer positions

MATLAB/Simulink™. The literature review made the case that there is a lack of available simulation twin technology for looking at system dynamic performance during the actuation of railway track switches. The approach has been demonstrated, by applying it to a REPOINT switch (a potential future track switch which is under development as part of an EU-funded research programme).

First, the proposed FE-based rail bending model was implemented and validated against steady-state results (obtained using a conventional approach). Next models for the actuators in the system were described, developed and integrated with the switch blades before the control system was added. The system requirements for a REPOINT switch were presented along with the steps in the design of the closed-loop control system to meet these requirements. The overall simulation with the designed controllers was then used to test overall performance. The results demonstrated that the system could meet the dynamic performance required, relatively easily. If short-term peaks in current (over 80% of the maximum current) are deemed appropriate the switch could operate significantly faster than required. The

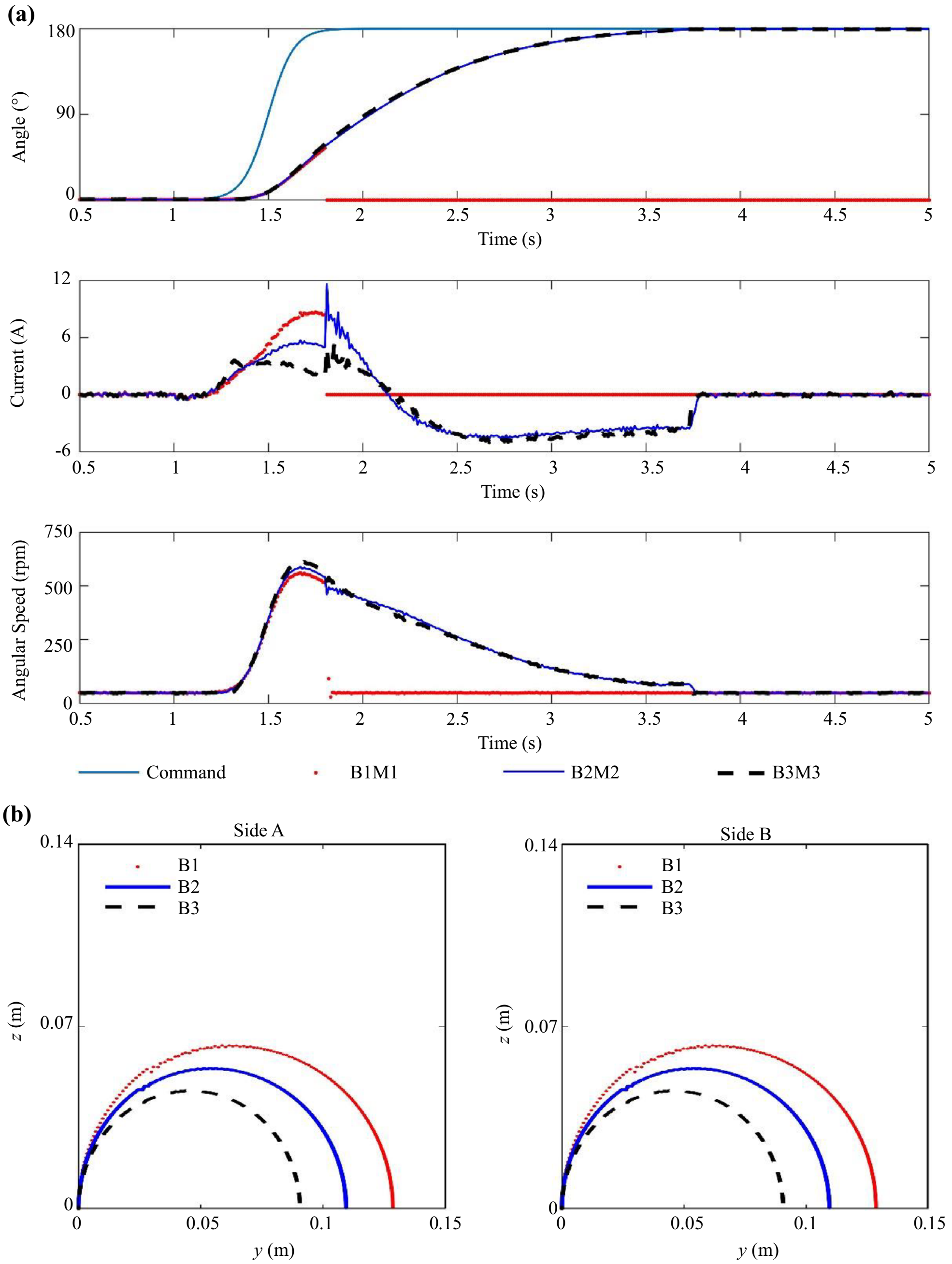

Fig. 12 Performance of the switch for designed failure case: **a** actuator performances; **b** movement of the rails at bearer positions

REPOINT switch incorporates build-in redundancy to allow tolerance of actuator faults; the simulation results for post-fault operation demonstrated that the switch was able to continue operating appropriately after such an actuator fault.

For the future, this modelling framework can be used (with modifications where necessary) to model other track switch designs and to evaluate their dynamic performance during switching. This presents an opportunity for the designers of existing switches to test the proposed actuation (switch machine) designs and optimize motor sizing. It also presents an opportunity to model other novel track switch concepts which might involve bending switch blades in 2D—as here with REPOINT—but could equally well be constrained to operate only in the 1D (horizontal plain).

Appendix A: Finite element formulation

$$\boldsymbol{M}^{\mathrm{G}} = \begin{bmatrix} \boldsymbol{M}_{11}^{1} & \boldsymbol{M}_{12}^{1} & 0 & \cdots & \cdots & 0 \\ \boldsymbol{M}_{21}^{1} & \boldsymbol{M}_{11}^{1} + \boldsymbol{M}_{22}^{2} & \boldsymbol{M}_{12}^{2} & \cdots & \cdots & \vdots \\ 0 & \boldsymbol{M}_{21}^{2} & \boldsymbol{M}_{22}^{2} + \boldsymbol{M}_{11}^{3} & \cdots & \cdots & \vdots \\ \vdots & \vdots & \ddots & \ddots & \vdots & \vdots \\ \vdots & \cdots & \cdots & \cdots & \boldsymbol{M}_{22}^{N-1} + \boldsymbol{M}_{11}^{N} & \boldsymbol{M}_{12}^{N} \\ 0 & \cdots & \cdots & \cdots & \boldsymbol{M}_{21}^{N} & \boldsymbol{M}_{22}^{N} \end{bmatrix},$$

$$\boldsymbol{K}^{\mathrm{G}} = \begin{bmatrix} \boldsymbol{K}_{11}^{1} & \boldsymbol{K}_{12}^{1} & 0 & \cdots & \cdots & 0 \\ K_{21}^{1} & K_{11}^{1} + K_{22}^{2} & \boldsymbol{K}_{12}^{2} & \cdots & \cdots & \vdots \\ 0 & \boldsymbol{K}_{21}^{2} & \boldsymbol{K}_{22}^{2} + \boldsymbol{K}_{11}^{3} & \cdots & \cdots & \vdots \\ \vdots & \vdots & \ddots & \ddots & \vdots & \vdots \\ \vdots & \cdots & \cdots & \cdots & \boldsymbol{K}_{22}^{N-1} + \boldsymbol{K}_{11}^{N} & \boldsymbol{K}_{12}^{N} \\ 0 & \cdots & \cdots & \cdots & \boldsymbol{K}_{21}^{N} & \boldsymbol{K}_{22}^{N} \end{bmatrix},$$

$$\boldsymbol{K}_{11}^{1} = \frac{1}{l^3} \begin{bmatrix} Al^2 & 0 & 0 & 0 & 0 & 0 \\ 0 & \frac{12EI_z}{1+P_y} & 0 & 0 & 0 & \frac{6EI_z l}{1+P_y} \\ 0 & 0 & \frac{12EI_y}{1+P_z} & 0 & -\frac{6EI_y l}{1+P_z} & 0 \\ 0 & 0 & 0 & GI_t l^2 & 0 & 0 \\ 0 & 0 & -\frac{6EI_y l}{1+P_z} & 0 & \frac{EI_y l^2(4+P_z)}{1+P_z} & 0 \\ 0 & \frac{6EI_z l}{1+P_y} & 0 & 0 & 0 & \frac{EI_z l^2(4+P_y)}{1+P_y} \end{bmatrix},$$

$$\boldsymbol{M}_{11}^{1} = m_1 \begin{bmatrix} 1/3 & 0 & 0 & 0 & 0 & 0 \\ 0 & \frac{13}{35} + \frac{6I_z}{5Al^2} & 0 & 0 & 0 & \frac{11l}{210} + \frac{I_z}{10Al} \\ 0 & 0 & \frac{13}{35} + \frac{6I_z}{5Al^2} & 0 & -\frac{11l}{210} - \frac{I_y}{10Al} & 0 \\ 0 & 0 & 0 & \frac{I_p}{3A} & 0 & 0 \\ 0 & 0 & -\frac{11l}{210} - \frac{I_y}{10Al} & 0 & \frac{l^2}{105} + \frac{2I_y}{15A} & 0 \\ 0 & \frac{11l}{210} + \frac{I_z}{10Al} & 0 & 0 & 0 & \frac{l^2}{105} + \frac{2I_z}{15A} \end{bmatrix},$$

$$\boldsymbol{M}_{12}^{1} = {\boldsymbol{M}_{21}^{1}}^{\mathrm{T}} = m_1 \begin{bmatrix} 1/6 & 0 & 0 & 0 & 0 & 0 \\ 0 & \frac{9}{70} - \frac{6I_z}{5Al^2} & 0 & 0 & 0 & \frac{13l}{420} - \frac{I_z}{10Al} \\ 0 & 0 & \frac{9}{70} - \frac{6I_z}{5Al^2} & 0 & -\frac{13l}{420} + \frac{I_y}{10Al} & 0 \\ 0 & 0 & 0 & \frac{I_p}{6A} & 0 & 0 \\ 0 & 0 & \frac{13l}{420} - \frac{I_y}{10Al} & 0 & -\frac{l^2}{140} - \frac{I_y}{15A} & 0 \\ 0 & -\frac{13l}{420} + \frac{I_z}{10Al} & 0 & 0 & 0 & -\frac{l^2}{140} - \frac{I_z}{15A} \end{bmatrix},$$

$$\boldsymbol{K}_{21}^{1} = {\boldsymbol{K}_{12}^{1}}^{\mathrm{T}} = \frac{1}{l^3} \begin{bmatrix} -EAl^2 & 0 & 0 & 0 & 0 & 0 \\ 0 & \frac{12EI_z}{1+P_y} & 0 & 0 & 0 & -\frac{6EI_z l}{1+P_y} \\ 0 & 0 & -\frac{12EI_y}{1+P_z} & 0 & \frac{6EI_y l}{1+P_z} & 0 \\ 0 & 0 & 0 & -GI_t l^2 & 0 & 0 \\ 0 & 0 & -\frac{6EI_y l}{1+P_z} & 0 & \frac{EI_y l^2(2-P_z)}{1+P_z} & 0 \\ 0 & \frac{6EI_z l}{1+P_y} & 0 & 0 & 0 & \frac{EI_z l^2(2-P_y)}{1+P_y} \end{bmatrix}.$$

Acknowledgements This research was supported by the European Union's 'Shift2Rail' through No. 826255 for the project IN2TRACK2: Research into enhanced track and switch and crossing system 2. The authors also gratefully acknowledge Network Rail for providing the drawings and data.

References

1. Bemment SD, Goodall RM, Dixon R et al (2017) Improving the reliability and availability of railway track switching by analysing historical failure data and introducing functionally redundant subsystems. Proc Inst Mech Eng F J Rail Rapid Transit 232(5):1407–1424
2. Rama D, Andrews JD (2013) A reliability analysis of railway switches. Proc Inst Mech Engt F J Rail Rapid Transit 227(4):344–363
3. Marquez FPG, Weston P, Roberts C (2007) Failure analysis and diagnostics for railway trackside equipment. Eng Fail Anal 14(8):1411–1426
4. Hamadache M, Dutta S, Olaby O et al (2019) On the fault detection and diagnosis of railway switch and crossing systems: an overview. Appl Sci 9(23):5129
5. Cao Y, Sun Y, Xie G et al (2021) A sound-based fault diagnosis method for railway point machines based on two-stage feature selection strategy and ensemble classifier. IEEE Trans Intell Transp Syst 23(8):12074–12083
6. Hu X, Cao Y, Sun Y, Tang T (2021) Railway automatic switch stationary contacts wear detection under few-shot occasions. IEEE Trans Intell Transp Syst 23(9):14893–14907
7. S-Code. http://www.s-code.info/. Accessed 1 May 2023
8. WIRAS. http://www.winterproofturnout.info/. Accessed 1 May 2023
9. Bemment SD, Ebinger E, Goodall RM et al (2017) Rethinking rail track switches for fault tolerance and enhanced performance. Proc Inst Mech Eng F J Rail Rapid Transit 231(9):1048–1065
10. Olaby O, Dutta S, Harrison T et al (2021) Realisation of a novel functionally redundant actuation system for a railway track-switch. Appl Sci 11(2):702
11. Farhat N, Ward CP, Goodall RM et al (2018) The benefits of mechatronically-guided railway vehicles: a multi-body physics simulation study. Mechatronics 51:115–126
12. Magalhaes H, Marques F, Antunes P et al (2022) Wheel-rail contact models in the presence of switches and crossings. Vehicle Syst Dyn 61(3):838–870
13. Bezin Y, Pålsson BA (2021) Multibody simulation benchmark for dynamic vehicle-track interaction in switches and crossings: modelling description and simulation tasks. Vehicle Syst Dyn 61(3):644–659
14. Bezin Y, Sarmiento-Carnevali M, Sichani MS et al (2019) Dynamic analysis and performance of a repoint track switch. Vehicle Syst Dyn 58(6):843–863
15. Shih JY, Ambur R, Boghani H et al (2020) A new switch and crossing design: introducing the back to back bistable switch. J Civil Eng Constr 9(4):175–186
16. Shih JY, Weston P, Entezami M et al (2022) Dynamic characteristics of a switch and crossing on the West Coast main line in the UK. Railw Eng Sci 30(2):183–203
17. Dutta S, Harrison T, Ward CP et al (2020) A new approach to railway track switch actuation: dynamic simulation and control of a self-adjusting switch. Proc Inst Mech Eng F J Rail Rapid Transit 234(7):779–790
18. Li L, Dutta S, Dixon R, Stewart E et al (2022) Railway track switch simulation: a new dynamic model for studying actuator and switch blade dynamics. Proc Inst Mech Eng F J Rail Rapid Transit 237(6):775–783
19. Rao SS (2021) Mechanical Vibrations (SI edition). Pearson Prentice Hall, Singapore
20. Panzer H, Hubele J, Eid R et al (2009) Generating a parametric finite element model of a 3d cantilever timoshenko beam using matlab. Lehrstuhl für Regelungstechnik, Erlangen
21. BEMMENT S, Goodall R, Ebinger E et al (2015) Extending maintenance intervals of track switches utilising multi-channel redundancy of actuation and sensing (infrastructure). In: The Proceedings of International Symposium on Seed-up and Service Technology for Railway and Maglev Systems: STECH, Chiba, pp 2E14–1
22. Bemment SD, Dixon R, Goodall RM (2016) Railway points, railway points operating apparatus and railway track crossing. US Patent 10260202
23. Ferreira AJ (2009) MATLAB codes for finite element analysis. Springer, New York
24. Ling X, Haldar A (2004) Element level system identification with unknown input with Rayleigh damping. J Eng Mech 130(8):877–885
25. Mohammad D, Khan N, Ramamurti V (1995) On the role of Rayleigh damping. J Sound Vib 185(2):207–218
26. Li Y, Ang KH, Chong GC (2006) PID control system analysis and design. IEEE Control Syst Mag 26(1):32–41
27. Garcia-Sanz M (2016) The Nyquist stability criterion in the Nichols chart. Int J Robust Nonlinear Control 26(12):2643–2651